MHD simulations of three-dimensional resistive reconnection in a cylindrical plasma column

E. Striani,[1][*] A. Mignone,[2][*] B. Vaidya,[2][*] G. Bodo[3] and A. Ferrari[1,2]

[1]*INFN Torino, via P. Giuria 1, I-10125 Torino, Italy*
[2]*Dipartimento di Fisica, via P. Giuria 1, I-10125 Torino, Italy*
[3]*Osservatorio Astronomico di INAF, Osservatorio Astrofisico di Torino, Strada Osservatorio 20, I-0025 Pino Torinese, Italy*

ABSTRACT

Magnetic reconnection is a plasma phenomenon where a topological rearrangement of magnetic field lines with opposite polarity results in dissipation of magnetic energy into heat, kinetic energy and particle acceleration. Such a phenomenon is considered as an efficient mechanism for energy release in laboratory and astrophysical plasmas. An important question is how to make the process fast enough to account for observed explosive energy releases. The classical model for steady state magnetic reconnection predicts reconnection times scaling as $S^{1/2}$ (where S is the Lundquist number) and yields time-scales several order of magnitude larger than the observed ones. Earlier two-dimensional MHD simulations showed that for large Lundquist number the reconnection time becomes independent of S ('fast reconnection' regime) due to the presence of the secondary tearing instability that takes place for $S \gtrsim 1 \times 10^4$. We report on our 3D MHD simulations of magnetic reconnection in a magnetically confined cylindrical plasma column under either a pressure balanced or a force-free equilibrium and compare the results with 2D simulations of a circular current sheet. We find that the 3D instabilities acting on these configurations result in a fragmentation of the initial current sheet in small filaments, leading to enhanced dissipation rate that becomes independent of the Lundquist number already at $S \simeq 1 \times 10^3$.

Key words: instabilities – magnetic reconnection – MHD – plasmas – galaxies: jets.

1 INTRODUCTION

Magnetic reconnection is a plasma phenomenon where a rapid rearrangement of magnetic fields of opposite polarity leads to the dissipation of the magnetic energy into heat, plasma kinetic energy and particle acceleration. In particular, magnetic reconnection is generally regarded as a mechanism to account for the fast (i.e. much shorter than the dynamical time-scale) and intense variability observed in many astrophysical environments, like active galactic nuclei (Giannios 2013) and pulsar wind nebulae (Cerutti et al. 2013). It is also likely to occur in space environments like solar flares and coronal mass ejection (Drake et al. 2006; Gordovskyy, Browning & Vekstein 2010a; Gordovskyy & Browning 2011). A measure of the conversion of magnetic energy into particle acceleration via magnetic reconnection in Earth's magnetosphere is reported in a recent paper of Burch et al. (2016). Finally, magnetic reconnection is responsible for sawtooth crashes that prevent the magnetic confinement in laboratory fusion experiments, such as tokamaks (Hastie 1997). The general features of steady state magnetic reconnection

are described by the theory of Sweet–Parker (Parker 1957; Sweet 1958), that proposed reconnection taking place in current sheets (localized regions of very intense currents where non-ideal effects become important) of length L and thickness δ. In this model the reconnection time-scales as $S^{1/2}$ (where $S = LV_A/\eta$, is the Lundquist number, L is the characteristic length of the field configuration, V_A is the Alfvén velocity and η is the resistivity). However, considering that the Lundquist number is very large in space, astrophysical and laboratory plasmas (e.g. $S \sim 10^{12}$–10^{14} in the solar corona and $S \sim 10^6$–10^8 in tokamaks, see Loureiro & Uzdensky 2016), the above mentioned scaling yields reconnection time-scales that are several order of magnitudes longer than observed. An attempt to solve this problem was suggested by Petschek (1964), whose model yields a logarithmic dependence of the reconnection rate on S. Petschek-like configuration and scaling are found in a recent relativistic resistive magnetohydrodynamic (MHD) simulation of Del Zanna et al. (2016). However, this regime was never observed in laboratory experiments.

The understanding of this time-scale problem was significantly improved using resistive MHD numerical simulations with large Lundquist number. Two-dimensional simulations (see, e.g. Samtaney et al. 2009; Huang & Bhattacharjee 2010, 2013; Loureiro et al. 2012) have shown that when $S > S_c \simeq 1 \times 10^4$, the current

[*] E-mail: striani@to.infn.it (ES); mignone@ph.unito.it (AM); bvaidya@unito.it (BV)

Here ρ, $\boldsymbol{v}$, $\boldsymbol{B}$ and p are, respectively, the fluid mass density, velocity, magnetic field and gas pressure. Proper closure is given by an isothermal equation of state, $p = c_s^2 \rho$ (where c_s is the isothermal speed of sound). The equations are solved in conservative form using a second-order Runge–Kutta time stepping with linear reconstruction and the Riemann solver of Roe (1981).

We consider a magnetized plasma column in which the azimuthal component takes the form

$$B_\phi(r) = B_0 \frac{r/a}{1 + (r/a)^2} \tanh\left(\frac{r - r_1}{w}\right),\tag{2}$$

where r_1 is the radius of field inversion and w is the width of the current sheet. Equation (2) has a maximum at $r = a$ where $B_\phi^{\max} = B_0/2$.

Our aim is to investigate the evolution of a cylindrical plasma column featuring a field in the form of equation (2). For simplicity, we will start by assuming an initial equilibrium configuration based on radial force balance. One should be aware, however, that such an equilibrium could not be realized as it is potentially prone to many types of instabilities, as we shall see. The issue of marginal equilibrium was recently addressed by Uzdensky & Loureiro (2016). Radial force balance is achieved by solving the radial component of the momentum equation, which reads

$$\frac{d\Pi}{dr} = -\frac{1}{2r^2} \frac{d}{dr}\left(r^2 B_\phi^2\right)\tag{3}$$

where $\Pi = p + B_z^2/2$. equation (3) has solution

$$\Pi = \Pi_0 - \left.\frac{B_\phi^2}{2}\right|_0^r - \int_0^r \frac{B_\phi^2}{r}\,dr,\tag{4}$$

where the integration constant,

$$\Pi_0 = p_0 + \left.\frac{B_z^2}{2}\right|_{r=0}.\tag{5}$$

The input parameters are the pitch P and the plasma β (a factor $1/\sqrt{4\pi}$ is absorbed in the definition of $\boldsymbol{B}$):

$$P = \left.\frac{r B_z}{B_\phi}\right|_{r=0}, \qquad \beta = \frac{2p}{|\boldsymbol{B}|^2}.\tag{6}$$

The plasma β is computed as the ratio of the on-axis gas pressure p_0 to the maximum B_ϕ value:

$$\beta = \frac{2p_0}{(B_\phi^{\max})^2} = \frac{8p_0}{B_0^2} \quad \Rightarrow \quad B_0 = \sqrt{\frac{8p_0}{\beta}}\tag{7}$$

We employ an isothermal equation of state ($p = \rho c_s^2$) and adopt periodic boundary conditions in the vertical (z) direction while equilibrium values are prescribed on the remaining sides. Lengths are measured in units of r_1, velocities in units of the isothermal sound speed (c_s), and ρ in units of the density at the axis. The computational domain is the Cartesian box with $x, y \in [-l/2, l/2]$ and $z \in [-l_z/2, l_z/2]$ where $l = 4r_1$. A random perturbation in v_x, v_y, v_z of amplitude 1 per cent of the sound speed is added. An additional perturbation comes from the $m = 4$ noise due to the spatial discretization of the cylindrical plasma column on a Cartesian grid.

2.1 Equilibrium balance

Two possible equilibrium configurations will be investigated: one in which the Lorentz force is balanced by a pressure gradient and the other in which the Lorentz force vanishes. We will refer to the first one as the pressure-balanced (PB) while to the other as FF.
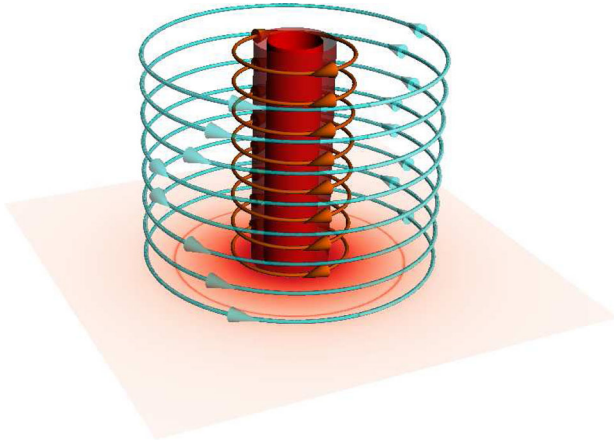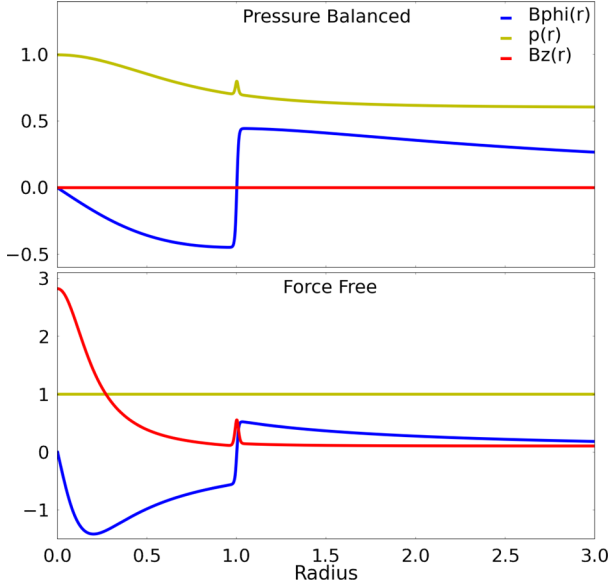

Figure 1. Contour rendering of the density showing the plasma column at $t = 0$ for the PB equilibrium. A slice of the density (pseudocolour rendering) on the xy plane ($z = -1$) is superimposed, showing the maximum of ρ at r_1 (see text). The red and blue circles show magnetic field lines of opposite polarity for B_ϕ.

sheet is subject to secondary tearing instability (Biskamp 1986), resulting in the fragmentation of the current sheet and formation of a large number of plasmoids. This leads to the so-called fast reconnection regime, where the reconnection rate becomes independent of the resistivity. Recent three-dimensional MHD simulations (Oishi et al. 2015) have further shown that 3D instabilities can trigger a 'fast reconnection' regime even for $S < S_c$.

In this work, we consider both 2D and 3D resistive MHD simulations of magnetically confined cylindrical plasma columns (see Fig. 1) featuring a current ring where the azimuthal component of magnetic field changes polarity. This field configuration was considered in Romanova & Lovelace (1992) and more recently in McKinney & Uzdensky (2012). We consider two initial equilibria: one in which radial force balance is established by a thermal pressure gradient and one in which the field is force-free (FF). The former can become unstable to pressure-driven instabilities while the latter is prone to the onset of current-driven modes. We then show that the presence of 3D plasma column instabilities results in a fragmentation of the initial current sheet and leads to a 'fast reconnection' regime also for $S \simeq 1 \times 10^3$.

This paper is organized as follows. In Section 2 we summarize the equations of resistive MHD used in the simulations and we present our model setup and initial conditions. In Section 3 we illustrate the results of our simulations. Finally in Section 4 we summarize and discuss our findings.

2 EQUATIONS AND MODEL SETUP

We solve the equations of resistive MHD listed below using the PLUTO code for astrophysical gas dynamics (Mignone et al. 2007, 2012):

$$\frac{\partial \rho}{\partial t} + \nabla \cdot (\rho \boldsymbol{v}) = 0$$

$$\rho\left[\frac{\partial \boldsymbol{v}}{\partial t} + (\boldsymbol{v} \cdot \nabla)\boldsymbol{v}\right] + \nabla p - (\nabla \times \boldsymbol{B}) \times \boldsymbol{B} = 0\tag{1}$$

$$\frac{\partial \boldsymbol{B}}{\partial t} - \nabla \times (\boldsymbol{v} \times \boldsymbol{B} - \eta \nabla \times \boldsymbol{B}) = 0$$

Figure 2. Radial profiles of B_ϕ, B_z and p for the PB (case PB-0) and FF (case FF-0.2) equilibrium configurations. In both cases the Lundquist number is $S = 2.4 \times 10^4$.

We set $l_z = 2r_1$ for the PB case while we choose $l_z = 4r_1$ for the FF case in order to accommodate the kink mode that has the maximum growth at long wavelength. The radial profiles of B_ϕ, B_z and p for both configurations are shown in Fig. 2. In each of the above configurations we also simulate runs without inversion in toroidal magnetic field, i.e. by setting the hyperbolic tangent term in equation (2) to unity. These runs without magnetic shear are denoted by the suffix -NS.

2.1.1 PB equilibrium

We assume a constant vertical field

$$B_z(r) = B_0 \frac{P}{a} \tag{8}$$

and solve equation (4) for the pressure p:

$$p(r) = p_0 - \left.\frac{B_\phi^2}{2}\right|_0^r - \int_0^r \frac{B_\phi^2}{r}\,dr\,, \tag{9}$$

where $p_0 = \rho c_s^2 = 1$ and the integral is solved numerically. This is a variable pitch profile. Without the magnetic shear the solution of equation (4) is

$$p(r) = p_0 - \frac{B_0^2}{2}\frac{r^2(2a^2 + r^2)}{(a^2 + r^2)^2}\,, \tag{10}$$

which has the constraint $p_0/B_0^2 > 1$. From equation (7) this implies $\beta > 4$.

The growth rates of unstable modes are typically of the order of c_s/R, where c_s is the sound speed and R is the jet radius (Longaretti 2008).

PB equilibria may be subject to pressure-driven instabilities (PDI) driven by perpendicular currents. They occur in plasma columns when the pressure force pushes the plasma out from the inside of the magnetic field lines curvature and their destabilizing term is proportional to the pressure gradient. This instability has a very short wavelength perpendicular to the magnetic field and long wavelengths parallel to the field (Freidberg 2014).

Table 1. Different 2D and 3D cases with PB and FF initial conditions along with their setup parameter values.

Case	Eq	Lundquist S ($\times 10^4$)	P	β	Resolution
PB-0-2D	PB	0.3	0.0	10	512×512
PB-0-2D	PB	1.1	0.0	10	1024×1024
PB-0-2D	PB	2.4	0.0	10	2048×2048
PB-0-2D	PB	3.4, 5.0, 6.6, 10	0.0	10	4096×4096
PB-0	PB	0.3, 0.7, 1.1	0.0	10	$512 \times 512 \times 256$
PB-0	PB	2.4	0.0	10	$1024 \times 1024 \times 512$
PB-0.5	PB	2.4	0.5	10	$1024 \times 1024 \times 512$
PB-0-NS	PB	2.4	0	10	$1024 \times 1024 \times 512$
FF-0.2	FF	0.3, 0.7, 1.1	0.2	1	$512 \times 512 \times 512$
FF-0.2	FF	2.4	0.2	1	$1024 \times 1024 \times 1024$
FF-10	FF	2.4	10	1	$1024 \times 1024 \times 1024$
FF-0.2-NS	FF	2.4	0.2	1	$1024 \times 1024 \times 1024$

2.1.2 FF equilibrium

We assume constant pressure $p(r) = p_0$ and solve equation (4) for the vertical field:

$$\frac{B_z^2(r)}{2} = \frac{B_{z0}^2}{2} - \left.\frac{B_\phi^2}{2}\right|_0^r - \int_0^r \frac{B_\phi^2}{r}\,dr. \tag{11}$$

Without the magnetic shear, the vertical field has the solution

$$B_z(r) = B_0 \sqrt{\frac{P^2(a^2 + r^2)^2 - r^2 a^2 (2a^2 + r^2)}{a^2(a^2 + r^2)^2}} \tag{12}$$

A necessary condition for the square root to be positive for $r \to \infty$ is therefore that $P \geq a$. In our simulations we choose $P = a$.

FF configurations may be prone to current-driven instabilities (CDI) driven by parallel currents. The $m = 1$ (where m is the azimuthal wavenumber) 'kink' mode is the most violent among CDI (Begelman 1998). In this context, three-dimensional MHD simulations of relativistic jets possessing an axial current have shown a prominent jet wiggling due to the growth of non-axial symmetric perturbations (see, e.g. Mignone et al. 2010, 2013).

3 RESULTS

We consider several simulations characterized by different choices of the Lundquist number $S = LV_A/\eta$ (where η is the resistivity, L is the characteristic length of the current sheet and $V_A = B/\sqrt{\rho}$ is the Alfvén velocity), plasma β, magnetic pitch and equilibrium configurations. The simulation cases along with their parameters are listed in Table 1 and are: case PB-0-2D (2D circular current sheet with pitch $P = 0$), case PB-0 (3D PB with $P = 0$), case PB-0-NS (same as the previous case, but without shear in magnetic field) case PB-0.5 (3D PB with $P = 0.5$), case FF-0.2 (3D FF with $P = 0.2$), case FF-0.2-NS (same as the previous case, but without shear in magnetic field) and case FF-10 (3D FF with $P = 10$). The simulation cases without inversion are not expected to dissipate magnetic energy via magnetic reconnection. They therefore serve as test cases to ensure that the observed dissipation of magnetic energy in runs with inversion arises from magnetic reconnection. For all of our simulations we fix the width of the current sheet to be $w = 0.01$. We set the plasma beta to be $\beta = 10$ for the PB cases and $\beta = 1$ for the FF. For each case, we express time in units of the Alfvén time-scale, defined as $t_A = 2\pi r_1/V_A$ where r_1 is our unit length and $V_A = \max(|\boldsymbol{B}|/\sqrt{\rho})$ over the entire computational domain at $t = 0$.

Our simulations for the PB and FF configurations stop at $t = 5.5t_A$ and $t = 10t_A$, respectively, when the evolution of magnetic reconnection and the instabilities allowed in each configuration is such that a prominent magnetic dissipation, up to 80 per cent of the initial magnetic energy, is reached. The resolutions are chosen so as to ensure that the numerical resistivity is significantly smaller than the physical resistivity. A preliminary 2D study was performed in order to find the optimal resolutions. We plotted the magnetic energy E_m versus t/t_A for a given Lundquist number and with different resolutions (512^2, 1024^2, 2048^2, 4096^2 and 8192^2), and we computed the time at which E_m reaches 80 per cent of the initial magnetic energy, t_{80}. We then choose the lowest resolution among those that yield the same value (within 10 per cent) of t_{80}.

3.1 Two-dimensional results

We begin our discussion by analysing the two-dimensional case. For the sake of reference, in Section 3.1.1 we estimate the reconnection rate in a simple Harris sheet configuration (Harris [1962]) for later comparison with the actual 2D circular current sheet (Section 3.1.2). The 2D circular current sheet is alike case 3D PB-0 case but does not include the *z*-direction.

3.1.1 Standard harris sheet

According to the Sweet–Parker theory, the reconnection rate η can be written as

$$\eta \equiv \frac{u_{\text{in}}}{u_{\text{out}}} \sim \frac{\delta}{L}\frac{1}{\sqrt{S}} \qquad (13)$$

where u_{in} and u_{out} are the inflow and outflow speeds, while δ and L are the current sheet's half width and half length, respectively. To compute δ we estimate the peak value of the current density at the reconnecting region, located at $y = 0$. We then define δ as the distance (along y) where J decreases by a factor $1/e$ of its peak value (*e*-folding distance), similarly to Mignone et al. ([2012]). In Fig. [3] we plot δ for various S (blue circles) along with a best fit. The Sweet–Parker scaling, $\sim S^{-1/2}$, is plotted with the black dashed line. For comparison, we calculated the reconnection rate by estimating the rate at which the magnetic energy dissipates, in a manner similar to Gordovskyy, Browning & Vekstein ([2010b]) and Oishi et al. ([2015]). In order to do so, we plot the temporal evolution of the total magnetic energy in the domain, and we compute the slope $\gamma = dE_m/dt$, where E_m is normalized to the initial value of the magnetic energy and t to the Alfvén time. The slopes are calculated at $t = t_A$ so as to ensure that magnetic reconnection has already started.[1] The dissipation rate, γ, for different values of S is shown in Fig. [3] (green circles). The two estimates of the reconnection rate are compatible and in agreement with the Sweet–Parker scaling. For convenience, in this work we will measure the dissipation rate γ, that is equivalent to the reconnection rate only for cases where reconnection is the dominant dissipating process. We will discuss the implications of this choice in the last paragraph.

3.1.2 Circular current sheet

The simulations exhibit different features for increasing values of the Lundquist number, estimated using a characteristic length $L =$
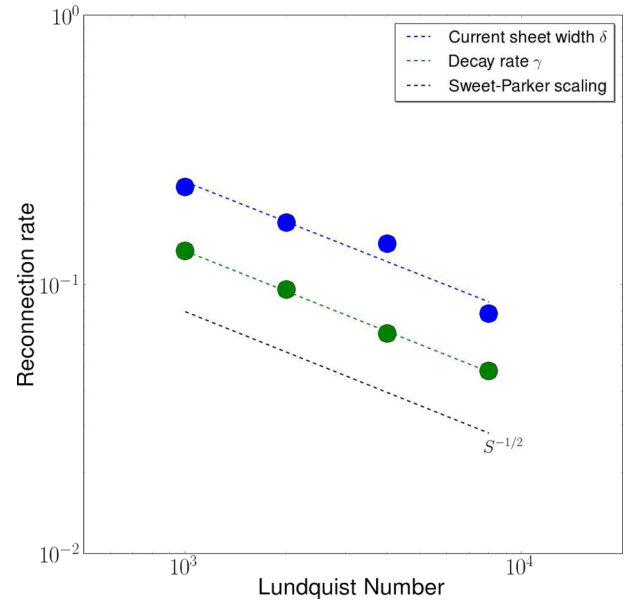

Figure 3. Reconnection rate η computed with two different methods: Blue: time average of δ as a function of S, along with a best fit (dashed line). Green: magnetic energy decay γ as a function of S, along with a best fit (dashed line). The Sweet–Parker scaling $\sim S^{-1/2}$ is plotted in black.

$2\pi r_1$. For $S = 1.7 \times 10^3$ the layer is highly diffusive, and there is no evidence of island formation. For larger S magnetic reconnection results in the formation of four plasmoids that further move along the curved current sheet and later merge into a larger island.

When $S > S_c \simeq 1\text{–}5 \times 10^4$ the simulations show evidences of multiple fragmentation of the current sheet by secondary tearing instability. Here we see the continuous hierarchical formation of islands between two already formed larger islands (see Fig. [4]). The islands further move away from the region of creation and feed the growth of a monster island (see Uzdensky, Loureiro & Schekochihin [2010]). The fragmentation of the layer ultimately results in formation of several small sized current sheets randomly oriented (see Fig. [4], right side) leading the system into a 'plasmoid turbulence' phase, as described in Loureiro et al. ([2012]). At this stage the current sheet configuration resembles that of the simulations of Kowal et al. (2009) and Loureiro et al. (2009).[2]

In Fig. [5] (upper panel) we show the temporal evolution of the average magnetic energy normalized to the initial magnetic energy for different values of the Lundquist number. For cases with $S \gtrsim 10^4$ the decay rate sharply increases at $t \simeq 3.2t_A$ (seen as steepening of the slope). This corresponds to the time when the secondary tearing instability sets in. Consequently we define two different phases in the temporal evolution of the magnetic energy: phase I that starts at the beginning of the simulation until the onset of the (plasmoid) instability, and phase II that starts after the onset of the instability (note that phase II is present only in the case where $S \geq 10^4$).

The central panel of Fig. [5] shows the temporal evolution of the average value of J^2 (denoted by $\langle J^2 \rangle$), where J is the current density. There is a clear distinction in the growth of $\langle J^2 \rangle$ with time between the two phases mentioned above, especially for higher values of S. The evolution of $\langle J^2 \rangle$ in phase I, after an initial transient, is typically flat for all values of S. As the instability sets in, a sharp rise is seen

---

[1] We have checked that the choice of the time at which slopes are computed has hardly noticeable differences on the results.

[2] We note, however, that these models focused on magnetic reconnection in the presence of a pre-existing, background turbulence.
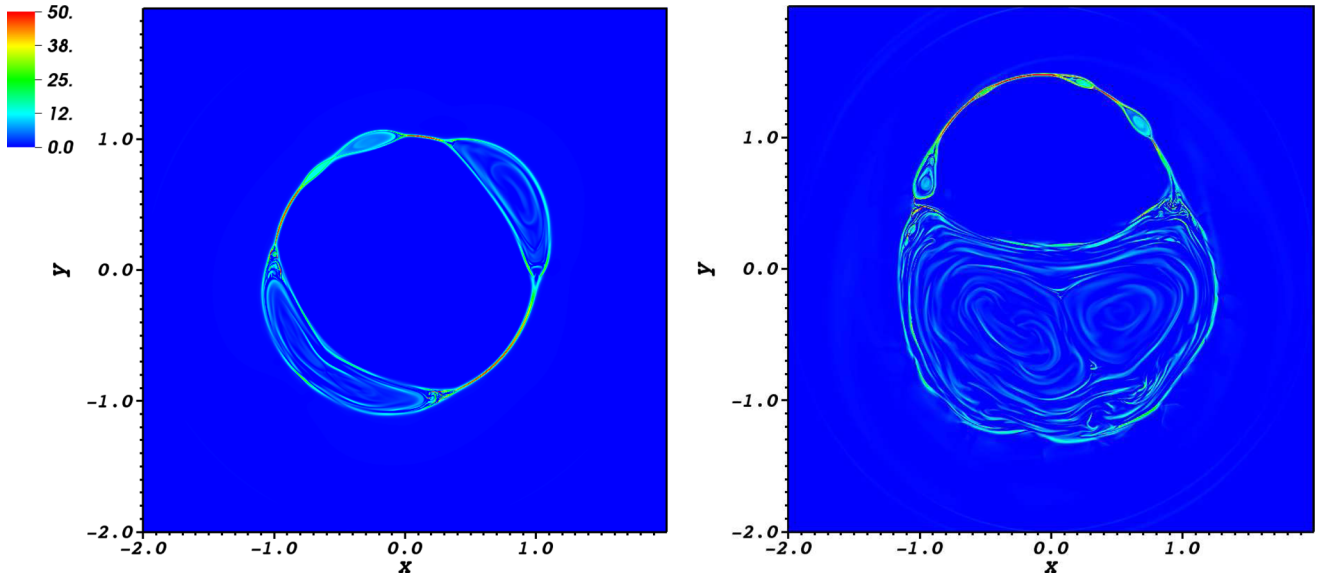
Figure 4. Pseudocolour rendering of the current density J_z for case 2D with $S = 1.0 \times 10^5$ at $t \simeq 2.5t_A$ (left) and $t \simeq 4.8t_A$ (right). We note the formation of multiple plasmoids and small-sized current sheets due to secondary tearing instability, in a manner similar to the 'plasmoid turbulence' described in Loureiro et al. (2012).
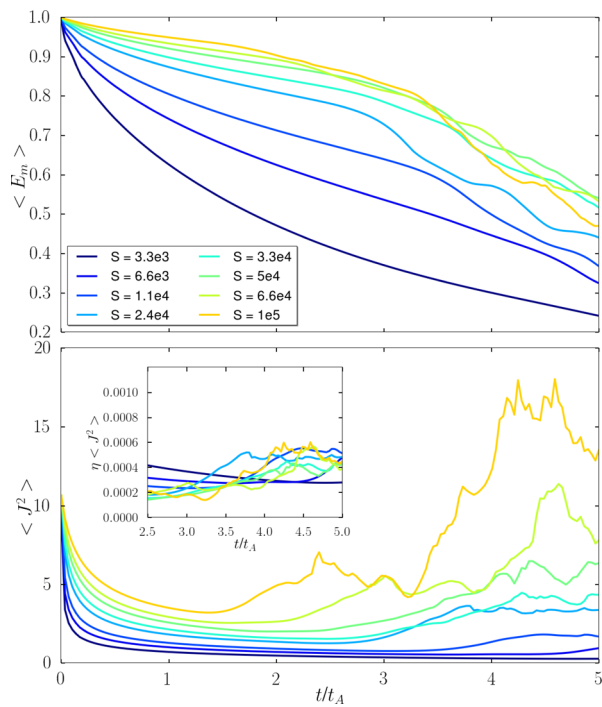

Figure 5. Two-dimensional circular current sheet. Top panel: temporal evolution of average magnetic energy E_m normalized to the initial magnetic energy for different values of the Lundquist number. Bottom panel: temporal evolution of $\langle J^2 \rangle$ for different values of the Lundquist number. Inset: temporal evolution of $\eta\langle J^2 \rangle$ for different Lundquist numbers.

Figure 6. Decay rate γ of the magnetic energy as a function of S for case PB-0-2D. For each S values γ is computed in phase I (circles) and phase 2 (triangles). The decay rate scales as $S^{-1/2}$ during phase I, and it is nearly independent on S in phase II.

By fitting the curves representing the temporal evolution of E_m during phase I and phase II, we can estimate the decay rate γ for the two phases. We show in Fig. 6 the decay rate for different values of S. We see that the dissipation rate follows the Sweet–Parker scaling during phase I (circles), and it is nearly independent of S in phase II (triangles). One can therefore identify phase I with a Sweet–Parker phase and phase II with a 'fast reconnection' regime. The rate at which magnetic energy is dissipated during the fast reconnection regime is $\sim 0.1t_A^{-1}$, consistent with rates reported by previous numerical results (e.g. Bhattacharjee et al. 2009; Huang & Bhattacharjee 2010; Loureiro & Uzdensky 2016) and the theoretical model of Uzdensky et al. (2010). We emphasize that this 'fast reconnection' regime is related to the plasmoid instability, that sets in only when $S \geq 1 \times 10^4$. These results confirm the findings of many earlier papers studying magnetic reconnection in a Harris current sheet for high S values (see, e.g. Huang & Bhattacharjee 2010, 2013), and extend them to the case of a circular current sheet.

in $\langle J^2 \rangle$ for values of $S \geq 10^4$, while for smaller S values it continues to remain flat. In particular for $S = 1 \times 10^5$ (yellow curve), $\langle J^2 \rangle$ increases steeply by a factor of four after $t = 3.2t_A$.

Finally, the inset panel of Fig. 5 shows the temporal evolution of the Ohmic heating. We note that while in phase I $\eta\langle J^2 \rangle$ decreases for larger values of S, in phase II it becomes independent on the Lundquist number.
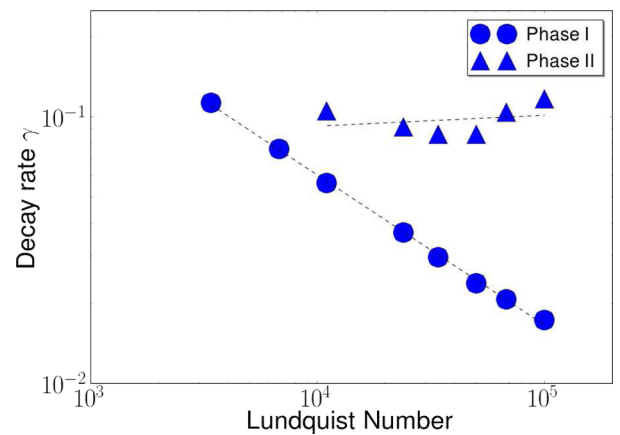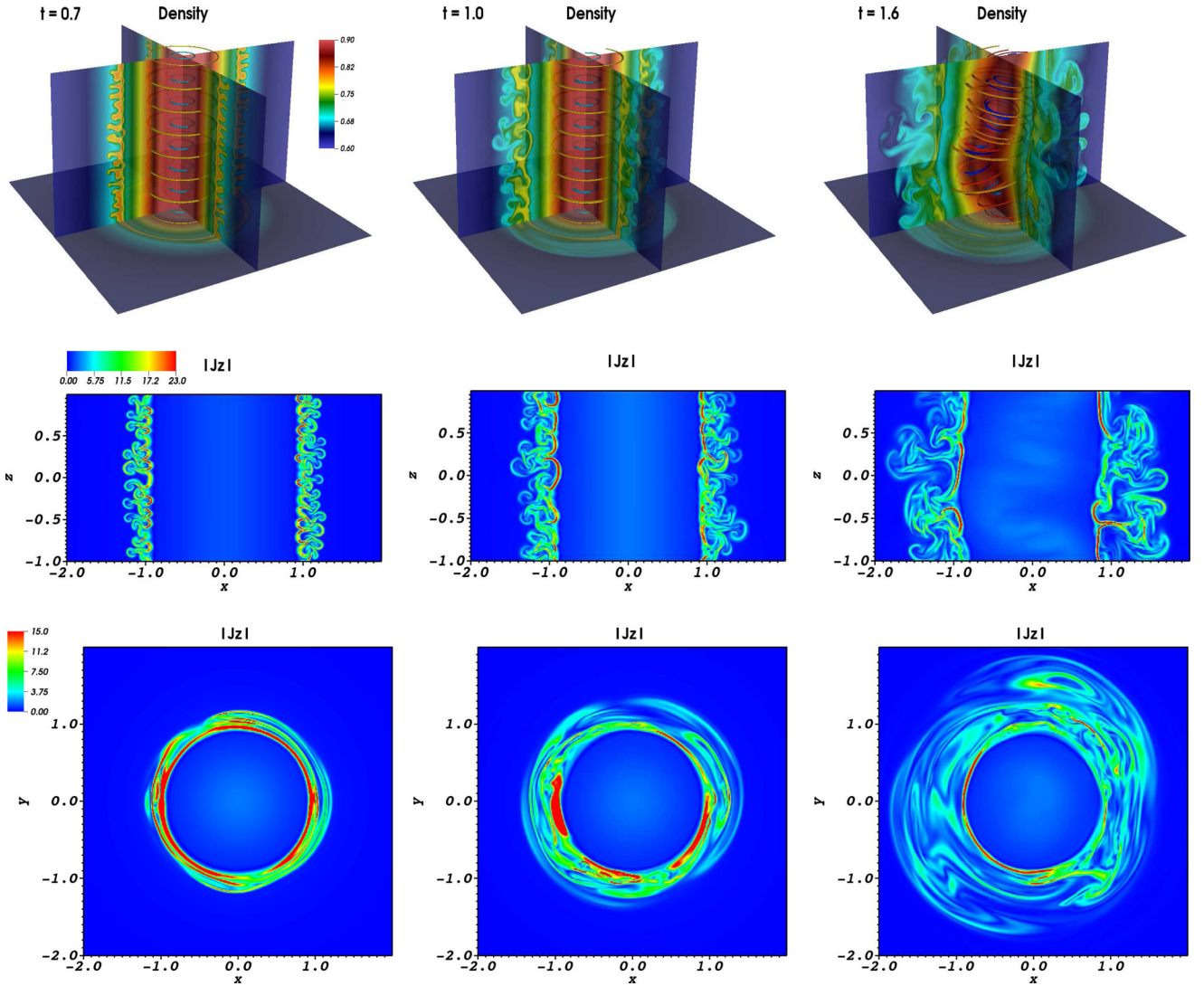
Figure 7. Snapshots for case PB-0 and $S = 2.4 \times 10^4$ for $t = 0.7t_A$, $t = 1.0t_A$, and $t = 1.6t_A$. We show the three-slice (pseudocolour rendering) of the density (top), the two-dimensional slice on the yz plane (at $x = 0$ of the current density centre), and the two-dimensional slice on the xy plane (at $z = 0.2$) (bottom).

3.2 Three-dimensional cases

3.2.1 3D pressure-balanced

The PB cases are unstable to PDI that triggers the formation of finger-like structures at the current sheet. The three-slice rendering of the density for case PB-0 with $S = 2.4 \times 10^4$ at $t = 0.7t_A$ (left), $t = 1.0t_A$ (centre) and $t = 1.6t_A$ (right) is shown in the top panels of Fig. 7, where one can observe the formation and growth of the fingers. These features start to form at $t \simeq 0.6t_A$ and continue to develop during the simulation. The growth of the PDI leads to the total disruption of the plasma column for $t > 3.5t_A$. The central panels of Fig. 7 show the 2D slice of the current density on the yz plane (at $x = 0$). Peaks of the current density in correspondence of the fingers can be noticed, pointing out that each of these features may become secondary current sheets where magnetic reconnection takes place. The 2D slice of the current density on the xy plane (at $z = 0.2$) is shown in the lower panels of Fig. 7. The formation of the fingers results in the fragmentation of the current sheet in the xy plane in several secondary and small-sized current sheets with high values of the current density. The length L' of these secondary

current sheets is much smaller than the size L of the original current sheet, therefore yielding an effective value of the Lundquist number $S' \propto L' \ll S$ and, finally, a dissipation rate that does not depend on S. This can be seen on the left side of Fig. 8 where the temporal evolution of the volume averaged magnetic energy (normalized to its initial value) for case PB-0 (red solid line), case PB-0.5 (red dashed line) and case PB-0-NS (red dotted line), along with case PB-2D (black solid line), is shown. The Lundquist number is $S = 2.4 \times 10^4$ for each of these plots. At early times the dissipation of the magnetic energy for case PB-0 overlaps with the 2D case. The curve is then characterized by a sharp change of the slope at $t \simeq 0.65t_A$, i.e. the time at which the finger-like features of the PDI start to form. In analogy with the PB-0-2D case, we define two different phases in the temporal evolution of the magnetic energy: phase I that starts at the beginning of the simulation until formation of the features of the pressure-driven instability, and phase II that begins after the formation of such features. In order to study the scaling of the dissipation rate for this case, we computed the decay rate $\gamma = dE_m/dt$ (see sec Section 3.1.1) by estimating the slope of the magnetic dissipation both in phase I and in phase II. Fig. 8
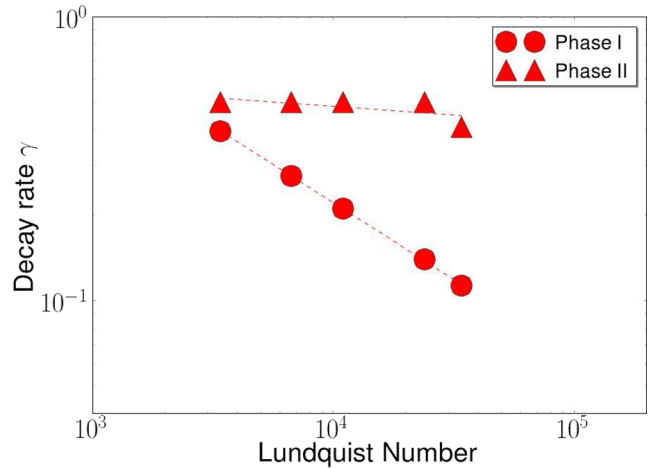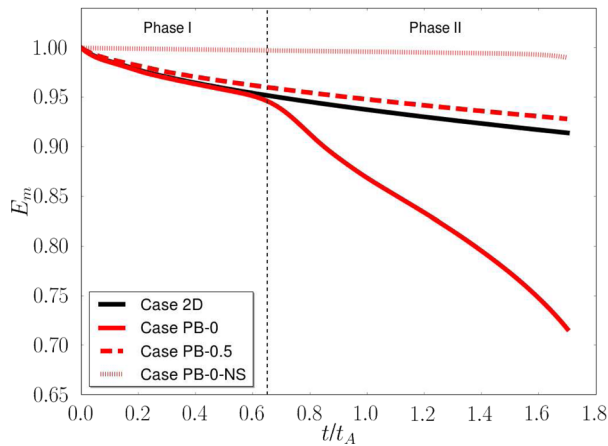
Figure 8. Left: temporal evolution of the volume averaged magnetic energy normalized to the initial magnetic energy for case PB-0 (red solid line), case PB-0.5 (dashed line) and case PB-0-NS (dotted line), along with case 2D (black). For all cases the Lundquist number is $S = 2.4 \times 10^4$. The black vertical line separates phase I and phase II for case PB-2D. Right: decay rate γ of the magnetic energy as a function of S for case PB-0. For each S value, γ is computed in phase I (circles) and phase 2 (triangles). We note that the decay rate follows the Sweet–Parker scaling during phase I, and is nearly independent on S in phase II.

(right-hand panel) shows the decay rate γ for different values of S and for the two different phases. In analogy with the 2D case, the dissipation rate follows the Sweet–Parker scaling in phase I (circles), and it is nearly independent on S (a linear fit yields a slope $\simeq 0.06$) in phase II (triangles). The rate of dissipation of magnetic energy during phase II is $\sim 0.5 t_A^{-1}$, somewhat larger than the rate obtained from 2D simulations (see section Section 3.1.2). The temporal evolution of the PDI for case PB-0.5 is much slower, as the increased pitch has a stabilizing effect on PDI. Consequently, this case does not show any features related to 3D instabilities throughout the simulation, and hints of finger formation are evident only at the very end of the simulation. The plasma column can be therefore considered as a replication along the z-direction of the 2D configuration of Section 3.1.2. This can be seen in the top panel of Fig. 8, where the dissipation of the (volume averaged) magnetic energy in the plasma column for this case (dashed line) overlaps with the 2D case. Finally, case PB-0-NS (dotted line) shows no sign of dissipation. The fragmentation of the layer due to the onset of the PDI and the consequent formation of small current-sheets observed for case PB-0 therefore yields a dissipation rate that does not depend on the Lundquist number. Differently from the 2D secondary tearing instability, the onset of PDI and its features do not depend on S, and the 'fast reconnection' regime holds also for $S \simeq 1 \times 10^3 < S_c$, when the secondary tearing instability is not present.

3.2.2 3D force-free

This configuration is unstable to CDI that favors the distortion of the plasma column due to the growth of the kink mode. This effect is visible in case FF-0.2, that exhibits a prominent bending of the plasma column that begins at $t \simeq 3 t_A$ and continues until the end of the simulation. The three-slice rendering of the current density superimposed with the contour of the density at $t = 6 t_A$, $t = 11 t_A$ and $t = 17 t_A$ for case FF-0.2 with $S = 2.4 \times 10^4$ is shown in the top panel of Fig. 9.

Along with the distortion of the plasma column by means of the kink mode, for $t > 3 t_A$ the current sheet along z breaks and forms plumes that grow and expand away from the central axis in the xz and yz planes. This can be seen also in the central panels of

Fig. 9, that shows the 2D slices on the yz plane (at $x = 0$) of the current density. To discriminate whether these features arise from the effect of the pressure-driven modes or the current driven modes, we estimated the value of $\chi = \cos^2(\theta)$ where θ is the angle between the current density and magnetic field vectors. For current-driven modes $\cos^2(\theta) = 1$, since currents and magnetic fields are parallel, while its value is zero for pressure-driven modes. Fig. 10, where χ for the FF-0.2 case at $t = 6 t_A$ is shown, exhibits many regions where $\cos^2(\theta) = 0$, implying that the plumes may originate from a secondary pressure-driven instability. The development of these features results in the fragmentation of the current sheet in the xy plane in several small current sheets. This can be seen in the lower panels of Fig. 9 where the 2D slices on the xy plane (at $z = -1$) of the current density is shown. Such a fragmentation ultimately results in formation of several randomly oriented filaments representing the onset of turbulent reconnection.

We show in Fig. 11 the temporal evolution of the volume averaged magnetic energy (normalized to its initial value) for case FF-0.2 with $S = 2.4 \times 10^4$ (solid line), case FF-0.2 with $S = 6.6 \times 10^3$ (dash–dotted line), case FF-10 with $S = 2.4 \times 10^4$ (dashed line), and case FF-0.2-NS with $S = 2.4 \times 10^4$ (dotted line). The dissipation of magnetic energy during the early stages of the simulation clearly depends on the Lundquist number, as can be seen comparing the two FF-0.2 cases with different S. The case without field inversion shows a negligible decrease of the magnetic energy, likely due to ohmic dissipation. All the configurations feature a sharp change in the decay rate between $4 t_A$ and $10 t_A$. This interval corresponds to the time when the CDI comes into play forming kinks in the plasma column. The decrease of magnetic energy in this interval can therefore be interpreted as conversion of magnetic energy into kinetic energy due to the onset of the kink instability. For $t > 10 t_A$ the magnetic energy decreases rapidly for both the FF-0.2 configurations with current sheet, with a rate that does not seem to depend on S. On the other hand, for the case without magnetic shear, the magnetic energy remains flat until $t \sim 20 t_A$.

In analogy with Sections 3.1.2 and 3.2.1, we define two different phases in the temporal evolution of the magnetic energy: phase I that starts at the beginning of the simulation until the time where the features of the plasma column instability set in, and phase II that begins after these instabilities sets in. The two phases are indicated
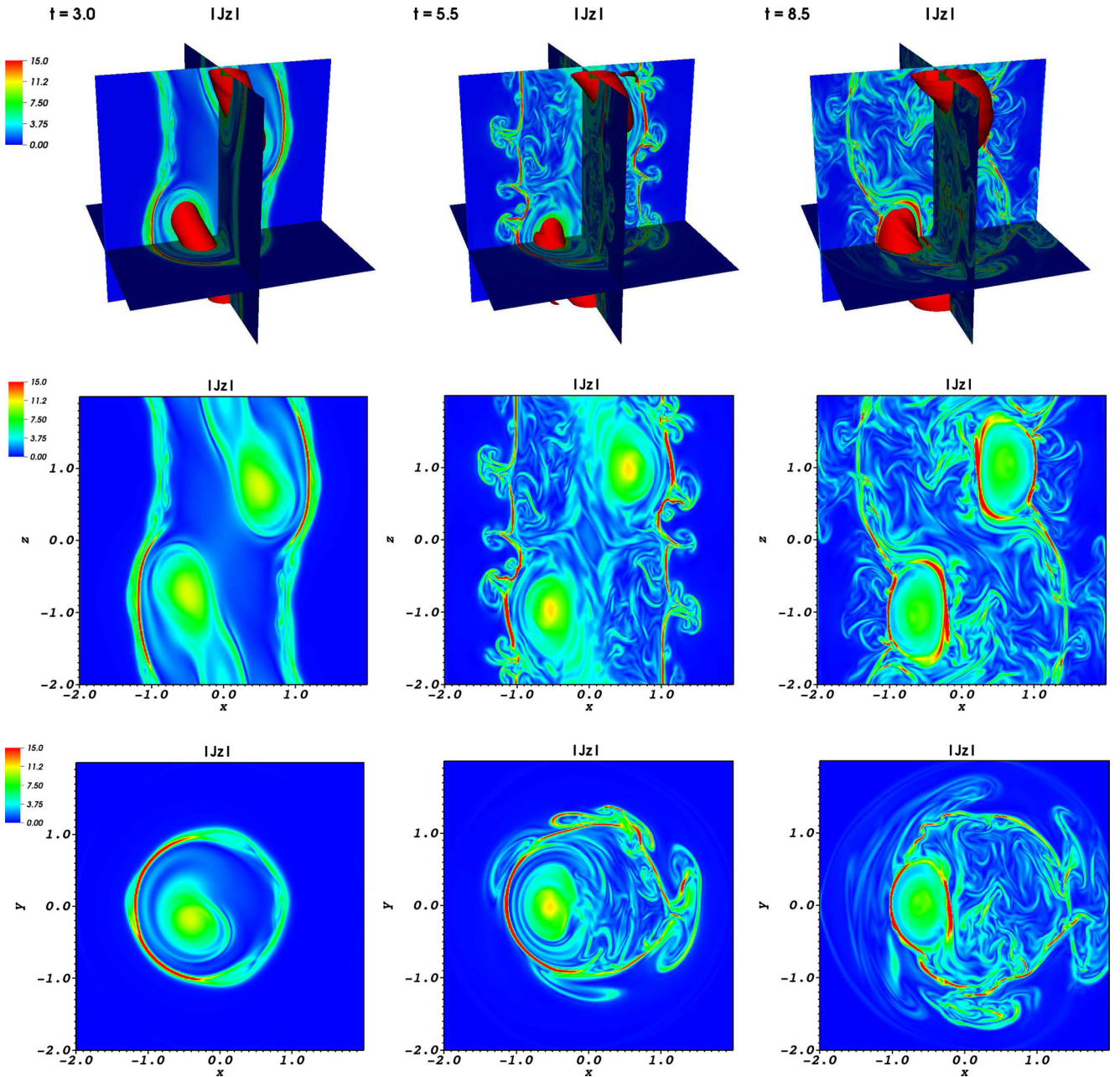
Figure 9. Snapshots for case FF-0.2 with $S = 2.4 \times 10^4$ at $t = 6t_A$, $t = 11t_A$ and $t = 17t_A$. We show the three-slice rendering of the current density superimposed to the contour rendering of the density (top), the two-dimensional slices on the xz plane (at $x = 0$) of the current density (centre), and the two-dimensional slices on the xy plane (at $z = -1$) of the current density (bottom).

by the dashed vertical lines on the left-hand panel of Fig. 11. We compute the decay rates in phase I and phase II for different S values for case FF-0.2, and show the dissipation rate obtained in such a way on the right-hand panel of Fig. 11. As for the 2D and PB cases, the dissipation rate in phase I follows the Sweet–Parker scaling (circles), while in phase II (triangles) the slope is nearly independent on S (a linear fit yields a slope $\simeq 0.1$). The rate of dissipation of magnetic energy during phase II is $\sim 0.1 t_A^{-1}$. In analogy with the 2D and 3D-PB cases, we note that this 'fast reconnection' regime sets in after the fragmentation of the layer.

Finally, case FF-10 shows a negligible decay of magnetic energy along the whole simulation, due to the fact that the higher pitch has a stabilizing effect on the 3D instabilities acting in this configuration.

4 SUMMARY AND DISCUSSION

We studied magnetic reconnection using three-dimensional resistive MHD simulations of a magnetically confined cylindrical plasma column featuring a circular current sheet. Different equilibrium conditions, including radial PB and an FF field, have been considered. Results have been compared with two-dimensional simulation of a circular current sheet.

Our 2D simulations generalize previous studies of planar current sheets to the cylindrical case. The main results from these simulations are listed below.

(i) At early stages (phase I), the magnetic dissipation rate in the current ring agrees with the Sweet–Parker scaling of $S^{-0.5}$.
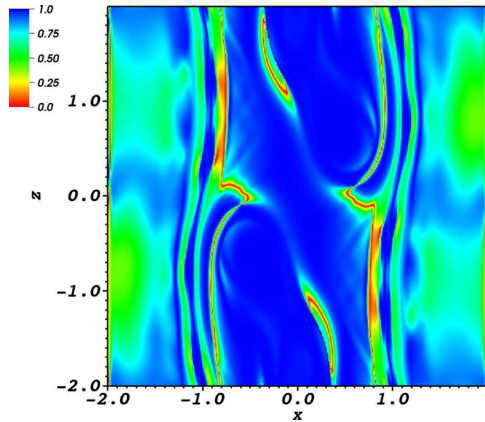
Figure 10. Two-dimensional slices on the *yz* plane (at $x = 0$) of $\chi = \cos^2(\theta)$ (see text) at $t = 6t_A$ for case FF-0.2. Regions where $\chi = 0$ are likely unstable to PDI that can be responsible for the features shown in the central panels of Fig. 9.

(ii) At later times (phase II) and for values of $S \gtrsim S_c \simeq 1 \times 10^4$, the current sheet is subjected to secondary tearing instability whereby continuous formation of plasmoids is observed. The formation of plasmoids leads to the fragmentation of the initial circular sheet into multiple small-sized current sheets. During this stage, the decay rate increases sharply, and becomes independent of S, revealing the transition to a regime of fast reconnection.

(iii) Eventually, the continuous formation and merging of plasmoids results in the random orientation of fragmented current-sheets that closely resemble the turbulent reconnection described by, e.g. Kowal et al. (2009), Loureiro et al. (2009) and Takamoto, Inoue & Lazarian (2015).

(iv) The rate of dissipation of magnetic energy during the fast reconnection regime is $\sim 0.1 t_A^{-1}$, consistent with previous numerical results of 2D reconnection.

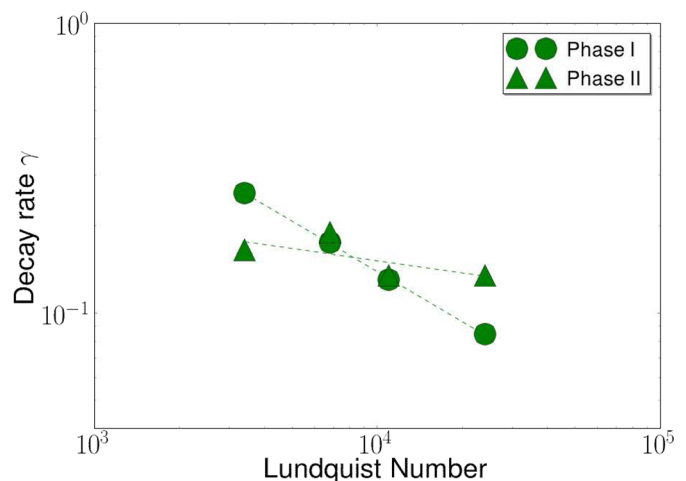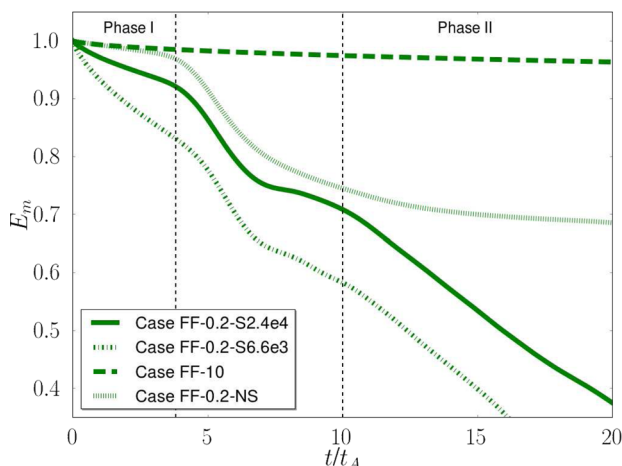In the three-dimensional case, our results can be summarized as follows.

(i) Similar to the 2D runs, the magnetic energy (during the initial phase) is dissipated at a rate which is consistent with Sweet–Parker scaling, $S^{-0.5}$.

(ii) At later times the plasma column becomes unstable to either pressure-driven or current-driven instabilities (depending on the initial equilibrium configuration), the onset of which does not depend on the Lundquist number. In runs with same set of parameters ($\beta = 10$ and $P = 0$), the 3D pressure-driven instability starts before the 2D secondary tearing mode. The growth of these instabilities causes the fragmentation of the original current ring into smaller secondary current sheets (see Figs 7 and 9).

(iii) At this time an increased magnetic dissipation is observed (phase II). The dissipation rate becomes independent of S and is of the order of $(\sim 0.1$–$0.5) t_A^{-1}$ (see Figs 8 and 11).

(iv) The dissipation rate starts to become independent of S for $S \simeq 10^{-3}$, a threshold value which is an order of magnitude smaller than the one obtained from 2D runs.

We point out that the dissipation rates reported here result from the interplay between magnetic reconnection and the turbulence induced by the instabilities arising in each configurations. This may lead to energy dissipation rates that are faster than the actual reconnection rate and could explain the differences between our findings ($\gtrsim 0.1 t_A^{-1}$) and the results reported in previous reference studies ($\sim 0.01 t_A^{-1}$). On the other hand, three-dimensional simulations without magnetic shear, that are not expected to develop magnetic reconnection, do not show relevant dissipation. In summary, we find that the 3D instabilities alone dissipate the magnetic energy inefficiently. However, they play a major role in enhancing the rate of magnetic dissipation in presence of reconnection.

We emphasize that the Lundquist numbers for the above 3D simulations lie in the range 10^3–10^4 and no formation of secondary tearing instability is observed. The 'fast reconnection' regime is, therefore, a mere effect of the 3D instabilities.

A similar effect was reported in recent 3D simulations by Oishi et al. (2015), where they attributed the early fast reconnection regime to an unspecified 3D instability. Our detailed analysis obtains consistent results in a different configuration (magnetically confined plasma column) and provides clear evidence that the onset

Figure 11. Left: temporal evolution of the volume averaged magnetic energy normalized to the initial magnetic energy for case FF-02 with $S = 2.4 \times 10^4$ (solid line), case FF-0.2 with $S = 6.6 \times 10^3$ (dash–dotted line), case FF-10 with $S = 2.4 \times 10^4$ (dashed line) and case FF-0.2-NS with $S = 2.4 \times 10^4$ (dotted line). The black vertical dashed lines indicates the beginning of phase II, where the decay rate γ for this case was computed. Right: decay rate γ of the magnetic energy as a function of S for case FF-0.2. For each case γ is computed in phase I (circles) and phase 2 (triangles). We note that the decay rate follows the Sweet–Parker scaling during phase I, and is nearly independent on S in phase II.

of 'fast reconnection' is triggered by well-known plasma instabilities (pressure- or current-driven). Our results are consistent with the complementary work by Singh, Mizuno & de Gouveia Dal Pino (2016) that show that kink instability in a relativistic rotating jet is able to trigger turbulence and magnetic reconnection.

Our results can be relevant in the context of MHD jets, where these instabilities are likely to operate. Typical astrophysical environments are active galactic nuclei, microquasars and pulsar wind nebulae. Here, magnetic reconnection has been recently invoked as an efficient mechanism to accelerate particles to non-thermal energies (Sironi & Spitkovsky 2014; de Gouveia Dal Pino & Kowal 2015) up to PeV energies (Cerutti et al. 2013). Plasma instabilities in jets, therefore, could trigger fast magnetic reconnection episodes (Lyubarsky 2012; Giannios 2013) that may account for the observed fast variability and non-thermal features in these astrophysical scenarios, like, e.g. the γ-ray flares from the Crab nebula (Striani et al. 2011; Tavani et al. 2011), or the very rapid variability, ~ 10 min, detected, e.g. in PKS 2155 (Aharonian et al. 2007) and PKS 1222 (Aleksić et al. 2011). Our results can, however, be applied only in the reference frame of the jet as no velocity shear has been considered. Besides, a more detailed analysis would require direct investigation of particle acceleration. These issues will be explored in forthcoming studies.

ACKNOWLEDGEMENTS

REFERENCES

Aharonian F. et al., 2007, ApJ, 664, L71
Aleksić J. et al., 2011, ApJ, 730, L8
Begelman M. C., 1998, ApJ, 493, 291
Bhattacharjee A., Huang Y.-M., Yang H., Rogers B., 2009, Phys. Plasmas, 16, 112102
Biskamp D., 1986, Phys. Fluids, 29, 1520
Burch J. L. et al., 2016, Science, 352, aaf2939
Cerutti B., Werner G. R., Uzdensky D. A., Begelman M. C., 2013, ApJ, 770, 147
de Gouveia Dal Pino E. M., Kowal G., 2015, Astrophysics and Space Science Library, Vol. 407, Magnetic Fields in Diffuse Media. Springer-Verlag, Berlin, Heidelberg, p. 373
Del Zanna L., Papini E., Landi S., Bugli M., Bucciantini N., 2016, MNRAS, 460, 3753
Drake J. F., Swisdak M., Schoeffler K. M., Rogers B. N., Kobayashi S., 2006, Geophys. Res. Lett., 33, L13105
Freidberg J. P., 2014, Ideal MHD. Cambridge Univ. Press, Cambridge
Giannios D., 2013, MNRAS, 431, 355
Gordovskyy M., Browning P. K., 2011, ApJ, 729, 101
Gordovskyy M., Browning P. K., Vekstein G. E., 2010a, A&A, 519, A21
Gordovskyy M., Browning P. K., Vekstein G. E., 2010b, ApJ, 720, 1603
Harris E. G., 1962, Il Nuovo Cimento, 23, 115
Hastie R. J., 1997, Ap&SS, 256, 177
Huang Y.-M., Bhattacharjee A., 2010, Phys. Plasmas, 17, 062104
Huang Y.-M., Bhattacharjee A., 2013, Phys. Plasmas, 20, 055702
Kowal G., Lazarian A., Vishniac E. T., Otmianowska-Mazur K., 2009, ApJ, 700, 63
Longaretti P.-Y., 2008, in Massaglia S., Bodo G., Mignone A., Rossi P., eds, Lecture Notes in Physics, Vol. 754, Jets From Young Stars III. Springer-Verlag, Berlin, p. 131
Loureiro N. F., Uzdensky D. A., 2016, Plasma Phys. Control. Fusion, 58, 014021
Loureiro N. F., Uzdensky D. A., Schekochihin A. A., Cowley S. C., Yousef T. A., 2009, MNRAS, 399, L146
Loureiro N. F., Samtaney R., Schekochihin A. A., Uzdensky D. A., 2012, Phys. Plasmas, 19, 042303
Lyubarsky Y. E., 2012, MNRAS, 427, 1497
McKinney J. C., Uzdensky D. A., 2012, MNRAS, 419, 573
Mignone A., Bodo G., Massaglia S., Matsakos T., Tesileanu O., Zanni C., Ferrari A., 2007, ApJS, 170, 228
Mignone A., Rossi P., Bodo G., Ferrari A., Massaglia S., 2010, MNRAS, 402, 7
Mignone A., Zanni C., Tzeferacos P., van Straalen B., Colella P., Bodo G., 2012, ApJS, 198, 7
Mignone A., Striani E., Tavani M., Ferrari A., 2013, MNRAS, 436, 1102
Oishi J. S., Mac Low M.-M., Collins D. C., Tamura M., 2015, ApJ, 806, L12
Parker E. N., 1957, J. Geophys. Res., 62, 509
Petschek H. E., 1964, NASA Spec. Publ., 50, 425
Roe P. L., 1981, J. Comput. Phys., 43, 357
Romanova M. M., Lovelace R. V. E., 1992, A&A, 262, 26
Samtaney R., Loureiro N. F., Uzdensky D. A., Schekochihin A. A., Cowley S. C., 2009, Phys. Rev. Lett., 103, 105004
Singh C. B., Mizuno Y., de Gouveia Dal Pino E. M., 2016, ApJ, 824, 48
Sironi L., Spitkovsky A., 2014, ApJ, 783, L21
Striani E. et al., 2011, ApJ, 741, L5
Sweet P. A., 1958, in Lehnert B., ed., Proc. IAU Symp. 6, Electromagnetic Phenomena in Cosmical Physics, p. 123
Takamoto M., Inoue T., Lazarian A., 2015, ApJ, 815, 16
Tavani M. et al., 2011, Science, 331, 736
Uzdensky D. A., Loureiro N. F., 2016, Phys. Rev. Lett., 116, 105003
Uzdensky D. A., Loureiro N. F., Schekochihin A. A., 2010, Phys. Rev. Lett., 105, 235002

This paper has been typeset from a TeX/LaTeX file prepared by the author.